

AD-A181 057

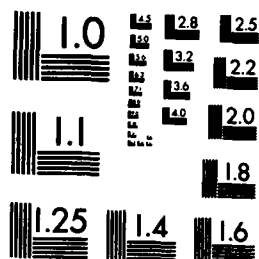
STRUCTURAL ANALYSIS OF FIBRE-REINFORCED METALLIC ROCKET
MOTOR CASES USING..(U) ROYAL ARMAMENT RESEARCH AND
DEVELOPMENT ESTABLISHMENT WALTHAM.. J MARGETSON ET AL.
DEC 86 RARDE-4/86 DRIC-BR-101447

1/1

UNCLASSIFIED

F/G 11/4

NL



MICROCOPY RESOLUTION TEST CHART
NATIONAL BUREAU OF STANDARDS-1963-A

AD-A181 057

UNLIMITED

MINISTRY OF DEFENCE

ROYAL ARMAMENT RESEARCH AND DEVELOPMENT ESTABLISHMENT

REPORT 4/86

Structural Analysis of Fibre-Reinforced Metallic Rocket
Motor Cases Using Finite-Element and Photoelastic Techniques

J Margetson
A Groves

Summary

Stress analysis procedures are presented for fibre-reinforced metallic rocket motor cases using finite-element and photoelastic techniques. These techniques enable analyses of the initial winding process, inertia and pressurisation due to firing to be performed. Certain simplifications and assumptions are introduced to resolve the complicating effects of the fibre overwind and the in-flight loadings. A comparison between the two methods for a typical motor is considered.

DTIC
ELECTE
S JUN 02 1987 D
E

UNLIMITED

CONTENTS

1	Introduction	3
2	Thin-Walled Section Analysis	3
	2.1 Overwinding Analysis	3
	2.2 Pressurisation Analysis	4
3	Thick-Walled Section Analysis	5
	3.1 Finite-Element Analysis	6
	3.2 Photoelastic Analysis	8
4	Comparison of Finite-Element and Photoelastic Stress Results	9
5	Conclusions	10
6	Acknowledgements	11
7	References	12

Table 1
Figures 1-12

Annex A Interface Pressure Calculation
Annex B Error Analysis



Accession For	
NTIS GRA&I	<input checked="" type="checkbox"/>
DTIC TAB	<input checked="" type="checkbox"/>
Unannounced	<input type="checkbox"/>
Justification	
By	
Distribution/	
Availability Codes	
Dist	Avail and/or Special
A-1	

UNLIMITED

1 INTRODUCTION

The selection of materials with high specific strengths, ie the ratio of ultimate tensile strength to specific gravity, is an important feature in the design of rocket motor cases. Maraging steel for example, with an ultimate tensile strength of 2200MPa and a specific gravity of 8, is one of the highest specific strength materials suitable for 'single' material designs. Attempts to use the even higher strength steels have, however, generated serious quality assurance problems associated, for instance, with their reduced ductility and some motors have failed in a brittle manner.

Alternatively, with the choice of suitable constituent materials, composite rocket motor cases can be manufactured with specific strengths exceeding that of any homogeneous design. A lightweight, load-bearing, aluminium tube, circumferentially reinforced with a high-strength polyamide fibre, is a particular example. Furthermore, if the fibre overwind is applied under tension, the case is put into compression. This defers the onset of tensile stresses and thereby effectively increases the firing pressure of the motor. In spite of these advantages prestraining has potential drawbacks. For example, experimental tests have shown that the strength and modulus of the fibre are reduced with prolonged periods of loading. Nevertheless, provided that adequate allowances are made for such degradations at the design stage, the considerable increase in the effective strength usually outweighs these drawbacks.

In the past the stress analysis of fibre-reinforced metallic rocket motor cases has been performed empirically (Ref 1), but during recent years the authors have been involved in the development of theoretical stressing procedures (Refs 2-6). This work has involved analyses of the initial winding process for both constant and variable winding strains, temperature excursions about the ambient winding temperature and the response of the motor when subjected to its firing pressure.

For the thin-walled cylindrical portion of the motor analytical stress solutions have been developed, whereas for the thicker and geometrically more complex regions of the motor finite-element procedures have been applied. Photoelastic stress analysis procedures have also been developed for fibre-reinforced rocket motor cases (Refs 7-8) so that the three-dimensional effects of the geometry, which cannot be readily analysed using the theoretical procedures, can be studied. In this report the theoretical and photoelastic techniques which have been used to analyse fibre-reinforced metallic rocket motor cases are reviewed and their respective stress solutions compared for a typical motor.

2 THIN-WALLED SECTION ANALYSIS

2.1 Overwinding Analysis

When n layers of fibre overwind are wound circumferentially at an initial winding strain ϵ_w on a metal case of radius R the case contracts radially owing to the external pressure of the overwind and is thereby put in compression. In the absence of an internal pressure the axial stress is

3
UNLIMITED

UNLIMITED

zero and, assuming that the radial contraction of the motor due to the application of each fibre layer is uniform through the overwound section, it has been shown (Ref 5) that the elastic pre-stress in the i 'th fibre layer and the case, $\sigma_{\theta f}^{(i,n)}$ and $\sigma_{\theta c}^{(n)}$ respectively, are given by

$$\sigma_{\theta f}^{(i,n)} = E_f \epsilon_w [1 - AF_i(A,n)] , \quad i = 1, 2, \dots, n , \quad (1)$$

$$\sigma_{\theta c}^{(n)} = -E_c \epsilon_w AF_1(A,n) , \quad (2)$$

where

$$F_i(A,n) = \sum_{j=1}^n \frac{1}{1+A_j} , \quad (3)$$

with the stiffness parameter A denoting

$$A = \frac{E_f t_f}{E_c t_c} . \quad (4)$$

In these equations the quantities E_f and E_c are the Young's modulus values for the fibres and case respectively, t_f is the effective thickness of a single fibre layer and t_c is the wall thickness of the metallic case.

For ease of computation it is convenient to approximate the summation term (ie $F_i(A,n)$) appearing in Equations 1 and 2 by an analytical expression. Using the Euler-Maclaurin formula (Ref 9) and neglecting all first-order terms and above, Equation 3 modifies to:

$$F_i(A,n) = \frac{1}{A} \ln \left[\frac{1+An}{1+Ai} \right] + \frac{1}{2(1+An)} + \frac{1}{2(1+Ai)} . \quad (5)$$

Detailed computations have shown that for typical A values (ie $A \geq 1$) the errors associated with this approximation are very small (of the order 0.05%).

Once the stresses in the fibres and the case have been derived, the corresponding elastic strains follow from the uniaxial Hookean stress-strain relationship.

2.2 Pressurisation Analysis

When the rocket motor case is subjected to its firing pressure it is a requirement that the motor must withstand all in-flight loads without failure or excessive deformation. Although these in-flight loads may contain components due to inertia and aero-heat, the dominant load will always be the firing pressure.

UNLIMITED

In the overwinding analysis the axial stress was zero. However, when the motor is subjected to its firing pressure the axial stress will, in general, be non-zero and is given by

$$\sigma_{zcp} = p \frac{(R^2 - R_e^2)}{2Rt_c}, \quad (6)$$

where R_e is the effective internal radius (Ref 3) of the throat insert, taking into account the non-uniform pressure distribution acting over the nozzle region. When an allowance for inertia effects is included, R_e will contain an additional component due to the axially varying inertia force.

The circumferential stresses in the fibres and the case are also modified when the motor is subjected to its firing pressure. It can be shown from a previous analysis (Ref 3) that the modified elastic circumferential

stresses in the i 'th fibre layer and the case, $\sigma_{\theta fp}^{(i,n)}$ and $\sigma_{\theta cp}^{(n)}$ respectively, are given by

$$\begin{aligned} \sigma_{\theta fp}^{(i,n)} &= E_f \epsilon_w [1 - A F_1(A, n)] \\ &+ \frac{pRA}{t_f(1+nA)} \left[1 - \frac{v_c}{2} \left[1 - \frac{R_e^2}{R^2} \right] \right], \quad i = 1, 2, \dots, n, \end{aligned} \quad (7)$$

$$\begin{aligned} \sigma_{\theta cp}^{(n)} &= -E_c \epsilon_w F_1(A, n) \\ &+ \frac{pR}{t_c(1+nA)} \left[1 + \frac{nv_c A}{2} \left[1 - \frac{R_e^2}{R^2} \right] \right], \end{aligned} \quad (8)$$

where v_c denotes the Poisson's ratio of the metallic case and p is the firing pressure.

As previously, once the stresses have been obtained, the elastic strains follow from the Hookean stress-strain relations.

3 THICK-WALLED SECTION ANALYSIS

In the preceding section simple analytical stress solutions were presented for the thin-walled sections of the motor. For the thick-walled and geometrically complex regions of the case a more sophisticated stress analysis approach is required.

For complex geometries the required stress analysis can be performed either theoretically or experimentally. For a theoretical analysis finite-

UNLIMITED

element techniques have to be adopted, whereas for an experimental study, strain gauging or photoelastic procedures can be applied. For experimental studies the photoelastic technique is usually preferred since it provides stress information at both the surface and interior points of the structure. It also has the advantage of providing detailed information of the stress variations in the regions of high stress concentrations taking into account full three-dimensional effects of the geometry.

The finite-element and photoelastic techniques are well documented (Refs 10 and 11) and are both capable of providing accurate stress predictions. However, the manner in which these techniques are applied to the overwound rocket motor case is not entirely straightforward due to the complicating effects of the fibre overwind and the in-flight loadings. Both methods of analysis are now discussed.

3.1 Finite-Element Analysis

For a rigorous stress analysis of the fibre-reinforced metallic rocket motor case it is necessary to employ specialised finite-element programs which provide facilities for accurately modelling the reinforcing properties of the fibre overwind and the pre-stress produced during winding. Although such programs are under development, they are not, as yet, available for use and it has been necessary to develop an alternative, albeit approximate, solution procedure using existing finite-element programs.

In the theory of finite-element stress analysis there exists a technique known as sub-structuring which enables the analysis of complex structures to be simplified. This technique involves the replacement of part of a structure by a set of equivalent forces, or displacements, applied to the interface boundary of the retained portion (Ref 10). For the overwound motor it follows therefore that the overwind can be removed and structurally represented by an external pressure equal in magnitude to the interface pressure between the first fibre layer and the metal case acting over the region previously occupied by the fibre overwind. The remaining structure, a homogeneous isotropic metal case, can then be analysed by any conventional axisymmetric finite-element program.

At this stage it would seem logical to evaluate the fibre/case interface pressure, p_b , by first calculating the circumferential stress, $\sigma_{\theta cp}^{(n)}$, from Equation 8 and then using the thin-walled cylinder equation to give

$$p_b = p - \frac{\sigma_{\theta cp}^{(n)} t_c}{R} \quad (9)$$

However, in situations where the interface pressure p_b and the applied internal pressure p are almost equal, it has been found from an error analysis for the circumferential stress (see Annex A) that as p_b approaches p a small error in the determination of p_b will lead to a large error in the circumferential stress calculation. Although the above equation yields an interface pressure within a few per cent of that predicted by the exact Lamé equations (Ref 14), serious errors were observed in the

UNLIMITED

finite-element stress solutions (in excess of twenty-five per cent) when this estimate of p_b was used. To ensure that accurate results are generated it is vital that the more precise relationship based on the Lamé equations (see Annex A)

$$p_b = p \frac{\left[\frac{2R_1^2}{E_c(R_b^2 - R_1^2)} - \frac{\nu_c(R_1^2 - R_e^2)}{E_c(R_b^2 - R_1^2)} \right]}{\left[\frac{R_b^2 + R_1^2}{E_c(R_b^2 - R_1^2)} + \frac{R_o^2 + R_b^2}{E_f(R_o^2 - R_b^2)} \right]} + \frac{E_c \epsilon_w A F_1(A, n) t_c}{R} \quad (10)$$

is used in the finite-element analysis, where R_1 and R_b denote respectively the internal and interface radii of the metallic case and R_o is the external radius of the overwound motor, ie $R_b + n t_f$.

In this approximate analysis the overwound section of the motor is divided into a series of cylinders, the lengths of which are selected to take into account the non-uniform axial stress variation due to inertia and possible variations in the total thickness of the fibre overwind and the case. For each cylinder the quantity R_e appearing in Equation 10 is calculated from Equation 6 in terms of the axial stress. This axial stress consists of two components, one which is proportional to the constant axially resolved integrated force due to the non-uniform internal pressure acting over the nozzle region, and one due to inertia, which is axially non-uniform. It should be noted that in the vicinity of the ends of the overwound section of the case the cylinder approximation is not strictly valid, but experimental results indicate that this method of analysis provides a reasonable working model for this theoretical study (see Section 4).

Since R_e is derived from the axial stress distribution it follows that the fibre/case interface pressure (see Eqn 10) is a function of the stress state being calculated. The solution process is therefore iterative, requiring an initial approximation for R_e , and hence the interface pressure, for each cylinder, followed by a succession of finite-element stress analyses with R_e and the interface pressure being updated between each iteration.

An initial approximation for R_e for each cylinder can be obtained by performing a finite-element stress analysis of the motor with all in-flight loads present, but with the overwind omitted. The derived axial stress solution is then used together with Equation 6 to obtain the required R_e values with the corresponding interfacial pressures p_b following from Equation 10.

Once the initial interface pressure has been calculated the isotropic finite-element analysis can be performed using, in this case, all in-flight loads together with the calculated interface pressures applied externally to the regions previously reinforced by the fibre overwind. An improved estimate for the axial stress is then obtained and from this a modified value for R_e for each cylinder is determined from Equation 6.

UNLIMITED

The updated interface pressures then follow from Equation 10. The whole process is repeated until the difference between successive stress solutions is less than a few per cent. Computations have shown that convergence is obtained within four or five iterations. This procedure is shown schematically in Figure 1.

3.2 Photoelastic Analysis

Nozzle stresses were determined experimentally using the three-dimensional 'frozen-stress' photoelastic technique (Refs 12 and 13). The models (twice full size) were machined from cast blanks of Araldite CT200 and a separate model was used for each form of loading (see below). The results were then combined by simple superposition to obtain the final stress state. Each stress-frozen model was sliced in both the meridional and circumferential planes and fringe readings were taken in a standard diffuse-light polariscope at the inner and outer edges of each slice. Standard techniques were used for material calibration and the motor stresses were obtained by proportional scaling as outlined below.

The approach for each of the four forms of loading studied is discussed below.

3.2.1 Inertial Loading

Stresses due to the inertia loadings resulting from a) the rocket motor's own mass and b) the fins were studied separately. The former were obtained from a model subjected to a simple dead weight axial loading (see Fig 2). The inertia load at any transverse plane in the motor is equal to the product of the mass of that part of the motor between the plane and the outlet, and its acceleration. In order to obtain the inertia stress at any particular transverse section of the motor, the model stresses were increased by a factor of four (to allow for model scale) and then by the ratio of the calculated inertia load at the section to the load applied to the model.

Stresses due to the fin-loading were obtained from a model subjected to dead weight loads applied to metal strips fitted into each of the four fin slots nearest the nozzle outlet. Motor stresses were obtained by proportionate scaling.

3.2.2 Pressure Loading

The non-uniform internal pressure in the motor was simulated in the model by a hydrostatic pressure loading using a combination of glycerine and Wood's metal (a low-melting-point alloy which is liquid at the stress-freezing temperature). The levels of the two 'liquids' inside and outside the model (see Fig 3) were such that a two-slope linearly varying pressure was obtained in the nozzle region of the motor and a constant pressure was obtained in the cylindrical portion. The relative densities of the liquids were such that, in relative terms, this pressure distribution was closely similar to that in the motor (Fig 4). Motor stresses were obtained from model stresses by simple scaling.

UNLIMITED

3.2.3 Overwinding

The pre-stress resulting from the overwinding process was simulated by shrink-fitting a series of Araldite rings on the parallel cylindrical section of the model. The ring/cylinder interference was chosen so as to give acceptable fringe orders in the stress-frozen model; the rings were heated to 135°C to allow them to be fitted on to the cylinder. An expression is available (Ref 3) for the mean circumferential stress produced in the cylinder in terms of the relevant motor variables. In obtaining the motor stresses from the model results, the model stresses were scaled by the ratio of the calculated mean circumferential stress in the motor to the observed mean circumferential stress in the cylindrical portion of the model.

4 COMPARISON OF FINITE ELEMENT AND PHOTOELASTIC STRESS RESULTS

Finite-element and photoelastic results have been compared for a typical motor case using representative material property data and in-flight loads (see Tab 1). A typical non-uniform pressure distribution acting on the inner surface of the motor and nozzle is shown by the solid line in Figure 4.

Because of the complexities associated with the motor geometry and in-flight loadings, certain simplifying assumptions were introduced into the finite-element analysis. The fin slots and location holes, which could not be modelled by the axisymmetric finite-element program, were omitted and replaced by solid sections in the finite-element mesh. Furthermore, to model the influence of the fins an element of representative mass was positioned adjacent to the fins' rear location point. The final finite-element mesh employed (see Fig 5) represented a compromise between solution accuracy and computer storage. Saint Venant's principle was invoked and the parallel section of the motor was truncated one diameter in length from the end of the overwound portion of the motor. A comparison between the finite-element and thin-walled cylinder solutions showed that the influence of the nozzle did not extend beyond that point.

The results of the finite-element and photoelastic stress analyses are presented in Figures 6 to 11. Selected plots of the circumferential and meridional stress distributions at the inner and outer surfaces of the motor for the same cross section are illustrated. A plot of the deformed shape obtained from the finite-element analysis is also presented in Figure 12.

In Figures 6 and 7 the circumferential and meridional stresses are plotted respectively for the overwinding and inertia loading conditions. These two quantities represent the dominant stresses which are produced for these two load cases. In Figure 6, where the circumferential stress distributions obtained from both analyses are plotted for the inner surface, the stress predictions are, in general, in good agreement. However, differences are observed for the region at the end of the overwound section which is close to the nozzle inlet. In the finite-element analysis the thin-walled cylinder equations were used to obtain the interface pressure p_i for this region and consequently 'end effect' errors may have been introduced.

UNLIMITED

This method of evaluating p_b is an intrinsic feature of the approximate finite-element procedure and the introduction of these errors is unavoidable.

In Figure 7, where meridional stress distributions at the inner surface of the rocket motor case are plotted for the inertia loading condition, it can be seen that the finite-element stress predictions are again in reasonable agreement with the photoelastic results. However, unexpected differences occurred in the thin-walled parallel section of the motor, and since the finite-element and analytical solutions are in close agreement this difference has probably been introduced through a deficiency in the inertia modelling used in the photoelastic analysis.

In the remaining figures (Figs 8-11) both the meridional and circumferential stress distributions are plotted for both the inner and outer surfaces for the combined loading case, ie overwinding, inertia and pressurisation. Since the pressurisation analysis is included in the combined loading analysis a separate assessment of that loading case has not been presented. Again, there is good agreement between the finite-element and photoelastic results. However, the following points are worth noting:

- a. In Figures 8 and 9, where the circumferential stress distributions are plotted for the inner and outer surfaces respectively, differences in the peak stresses are observed. These differences are attributable to the coarseness of the finite-element mesh employed adjacent to sudden changes in motor geometry and the three-dimensional effects of the fin slots and location holes included in the photoelastic analysis.
- b. For combined loading conditions there is also good agreement between the two stressing techniques for the prediction of the meridional stress distribution at the inner (see Fig 10) and outer (see Fig 11) surfaces. The differences which were present in the inertia analysis have been carried through into the combined loading analysis. The photoelastic predictions for the thin-walled section consequently differ slightly from that given by the finite-element solution.
- c. Although the interface pressure between the first fibre layer and the case can be evaluated theoretically, it is nevertheless an empirically unknown quantity. Consequently photoelastic stress solutions could not be obtained for the outer surface of the overwound portion of the motor.

5 CONCLUSIONS

Stress analysis procedures using the finite-element and photoelastic techniques for analysing fibre-reinforced metallic rocket motor cases have been presented. These techniques enabled analyses of the overwinding process, inertia and pressurisation due to firing to be performed. Certain simplifications and assumptions had to be introduced into both methods. When the two procedures were applied to the stress analysis of a typical overwound rocket motor case reasonable agreement was achieved for all load cases studied.

UNLIMITED

6 ACKNOWLEDGEMENTS

The authors would like to acknowledge the contributions of Professor P Stanley and Mr T E Thorpe (Simon Engineering, University of Manchester, UK) who have been involved in the development of the experimental work detailed in this paper and in the drafting of Section 3.2. The authors would also like to acknowledge F Phillis of Stress Engineering Services Ltd whose photoelastic stress results were used in the preparation of this report.

Technical discussions with Messrs Cook and Parratt of RARDE Waltham Abbey are also gratefully acknowledged.

UNLIMITED

7 REFERENCES

- 1 Unpublished MOD(PE) report.
- 2 Groves A Unpublished MOD(PE) report.
Margetson J
Stanley P
- 3 Stanley P Analytical Stress Solutions for Fibre-Reinforced
Margetson J Metallic Rocket Motor Cases. Int J Mech Sci, 26,
Groves A No 2, 1984, pp119-130.
- 4 Margetson J Stress Analysis of Metallic Rocket Motor Cases
Groves A Reinforced with a Viscoelastic Fibre Overwind.
Stanley P Accepted for publication in Int J Mech Sci, 1985.
- 5 Groves A Unpublished MOD(PE) report.
Margetson J
Stanley P
- 6 Margetson J Stress Analysis Procedures for the Design of
 Fibre-Reinforced Metallic Rocket Motor Cases.
 Paper AIAA-83-1330. AIAA/SAF/ASME 19th Joint
 Propulsion Conference, Seattle, Washington,
 June 1983.
- 7 Phillis F Unpublished Stress Engineering Services Ltd
 report.
- 8 Thorpe T E Unpublished University of Manchester report.
Stanley P
- 9 Scheid F Numerical Analysis. Schaums Outline Series,
 McGraw-Hill Book Company, 1968.
- 10 Zienkiewicz O C The Finite Element Method. 3rd Edn. McGraw-
 Hill Book Company Ltd, London, 1977.
- 11 Procht M M Photoelasticity I and II, John Wiley and Sons,
 New York, 1941.
- 12 Durelli A J Introduction of Photomechanics. Prentice-Hall
Riley W F Inc, Englewood Cliffs, NJ, 1965.
- 13 Stanley P Three-Dimensional Photoelastic Stress Analysis;
 Techniques and Applications. Experimentelle
 Technik der Physik, XVI, 1968, pp201-216.
- 14 Tomoshenko S Theory of Elasticity. 3rd Edn, McGraw-Hill,
Goodier J N New York, 1970.

Reports quoted are not necessarily available to members of the public or to commercial organisations.

UNLIMITED

TABLE 1 Motor Case Material Properties and In-Flight Loads Data

Young's modulus	Fibre : 93GPa Case : 73.2GPa
Poisson's ratio of case	: 0.3
Yield stress of case	: 470MPa
Density of case	: 2700kg/m ³
Thicknesses	Fibre : 0.11mm Case : 1.95mm
Radii	Interface : 46.9mm Effective : 34.6mm
Applied winding strain	: 0.33%
Number of layers	: 20

UNLIMITED

FIG. 1

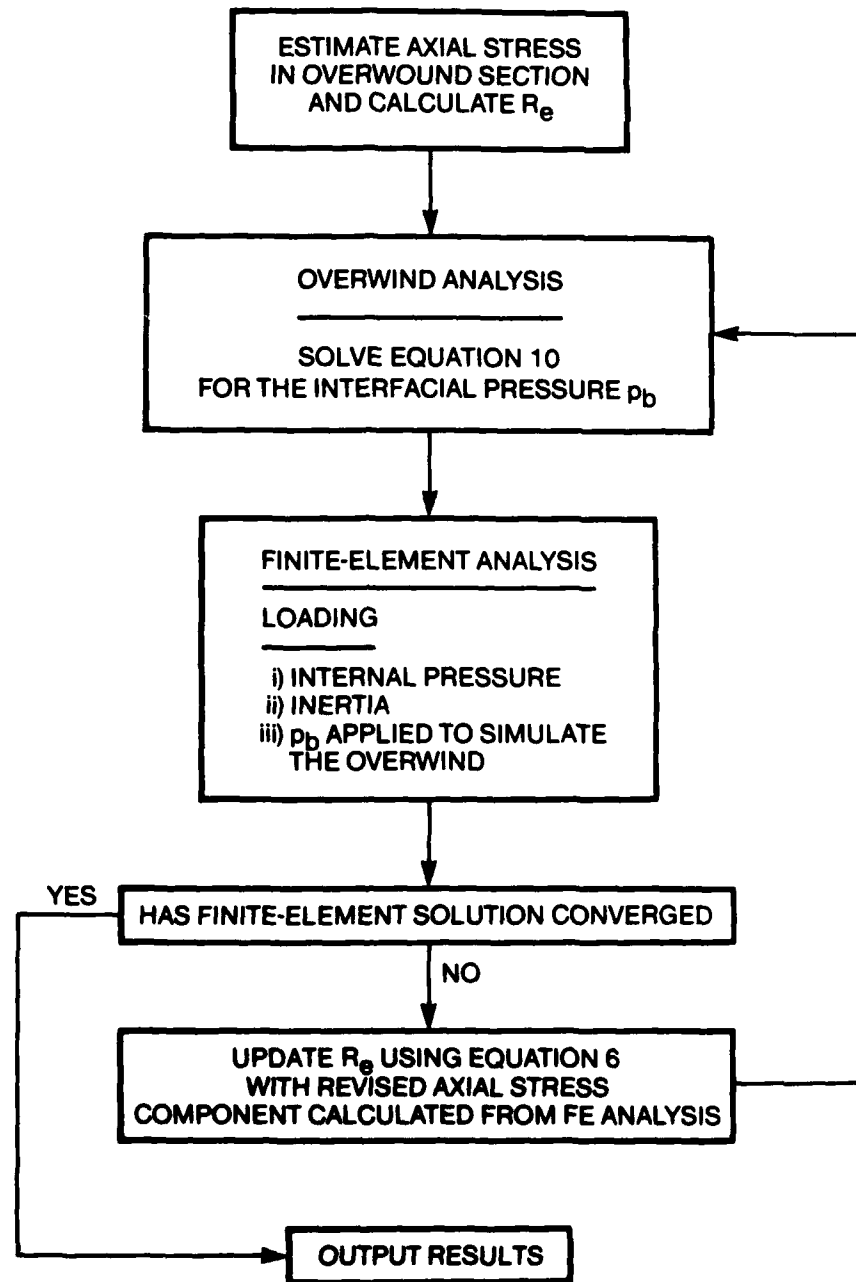


FIG. 1 APPROXIMATE FINITE-ELEMENT SOLUTION PROCEDURE

UNLIMITED

UNLIMITED

FIG. 2

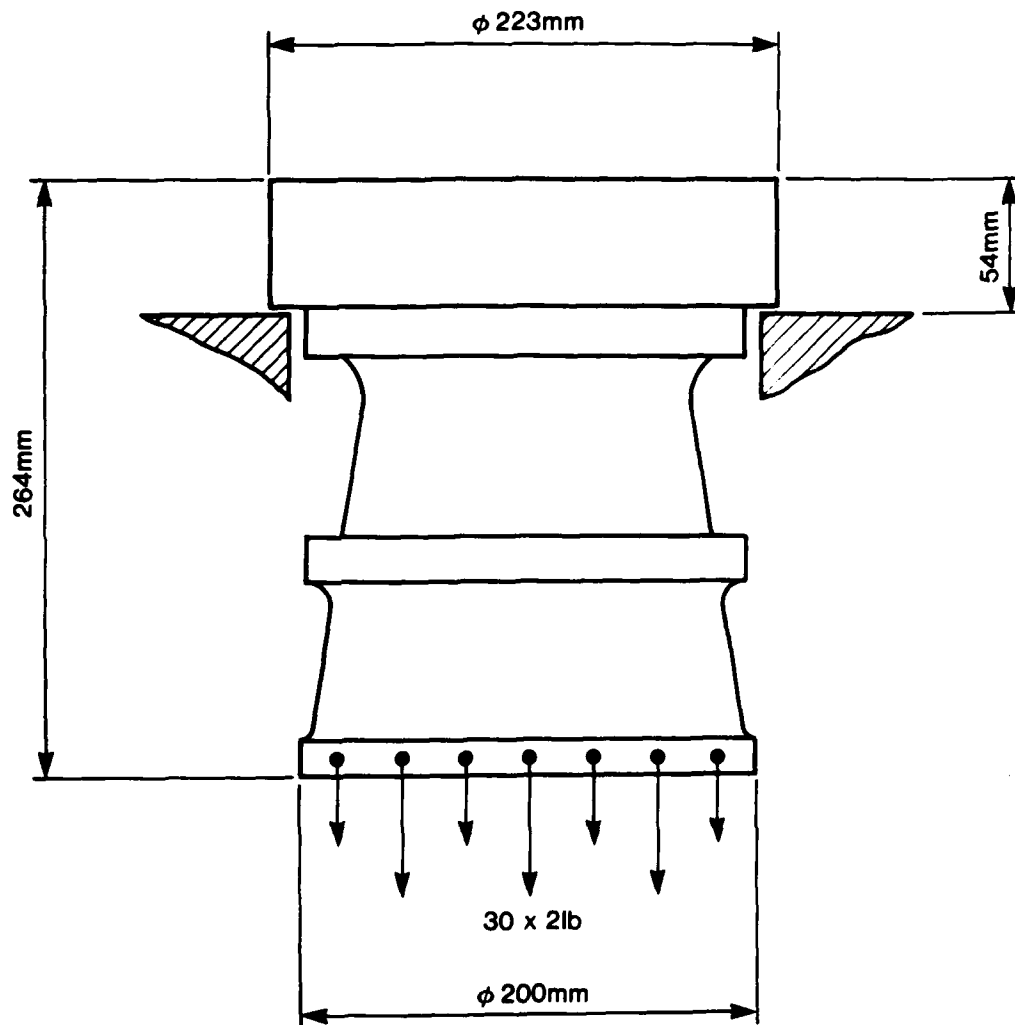


FIG. 2 INERTIA LOADING SIMULATION PROCEDURE

UNLIMITED

UNLIMITED

FIG. 3

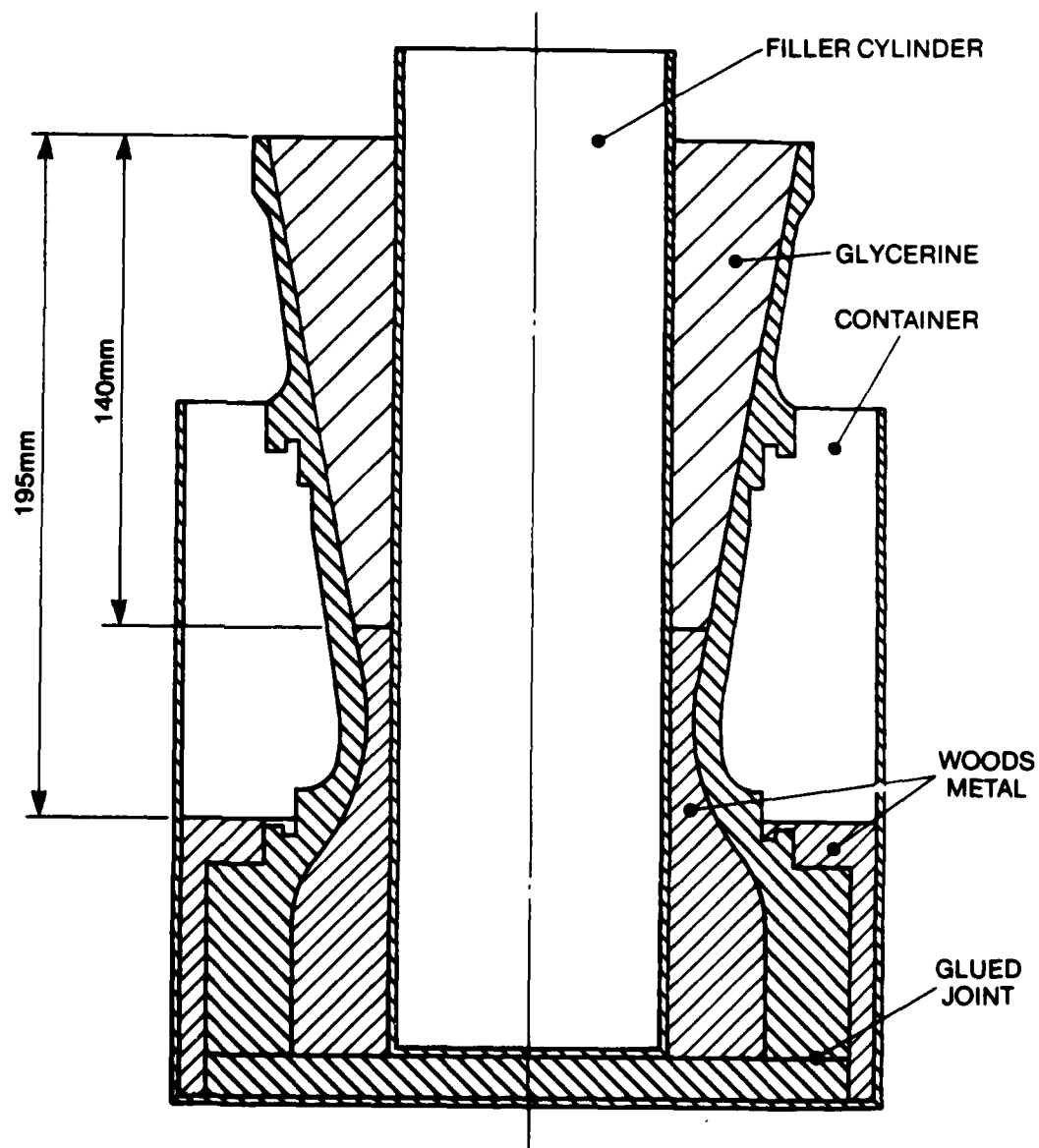


FIG. 3 NON-UNIFORM PRESSURE SIMULATION PROCEDURE

UNLIMITED

UNLIMITED

FIG. 4

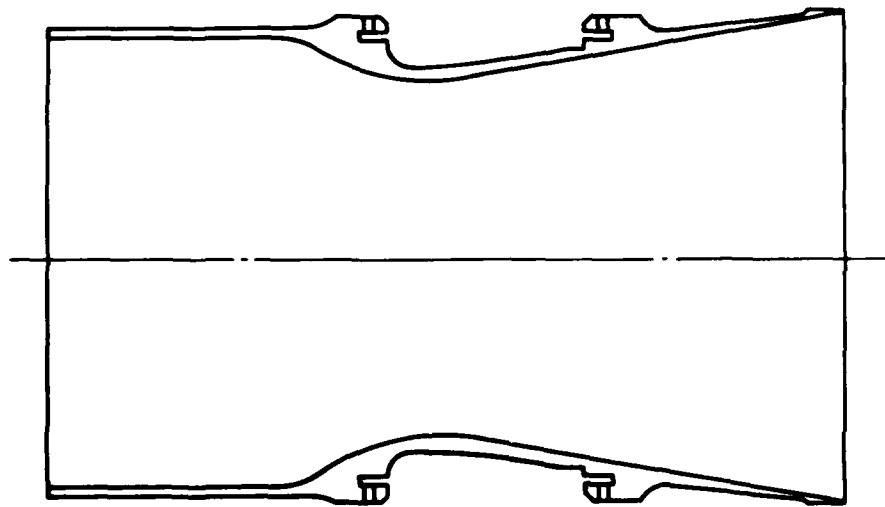
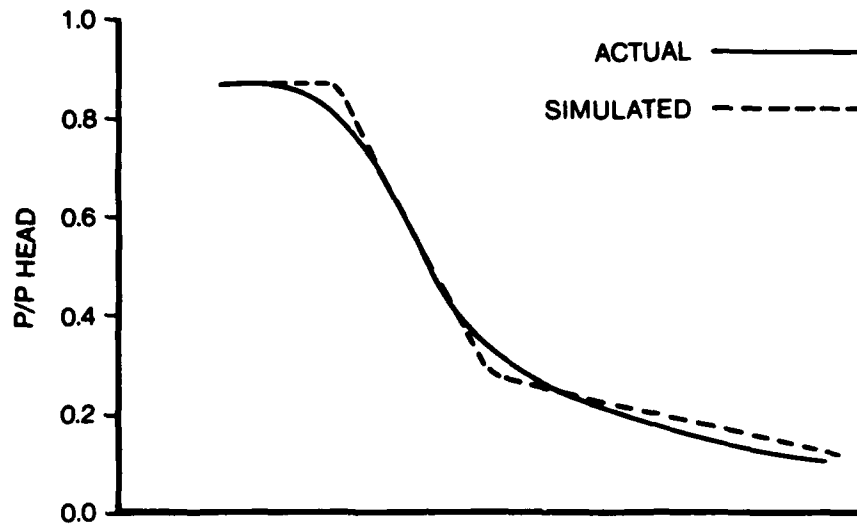


FIG. 4 PRESSURE DISTRIBUTION THROUGH NOZZLE

UNLIMITED

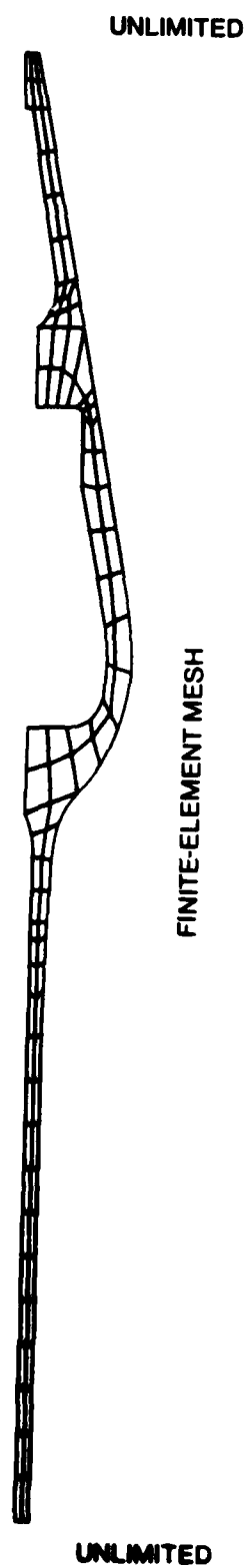


FIG. 5

FIG. 5 FINITE-ELEMENT MESH

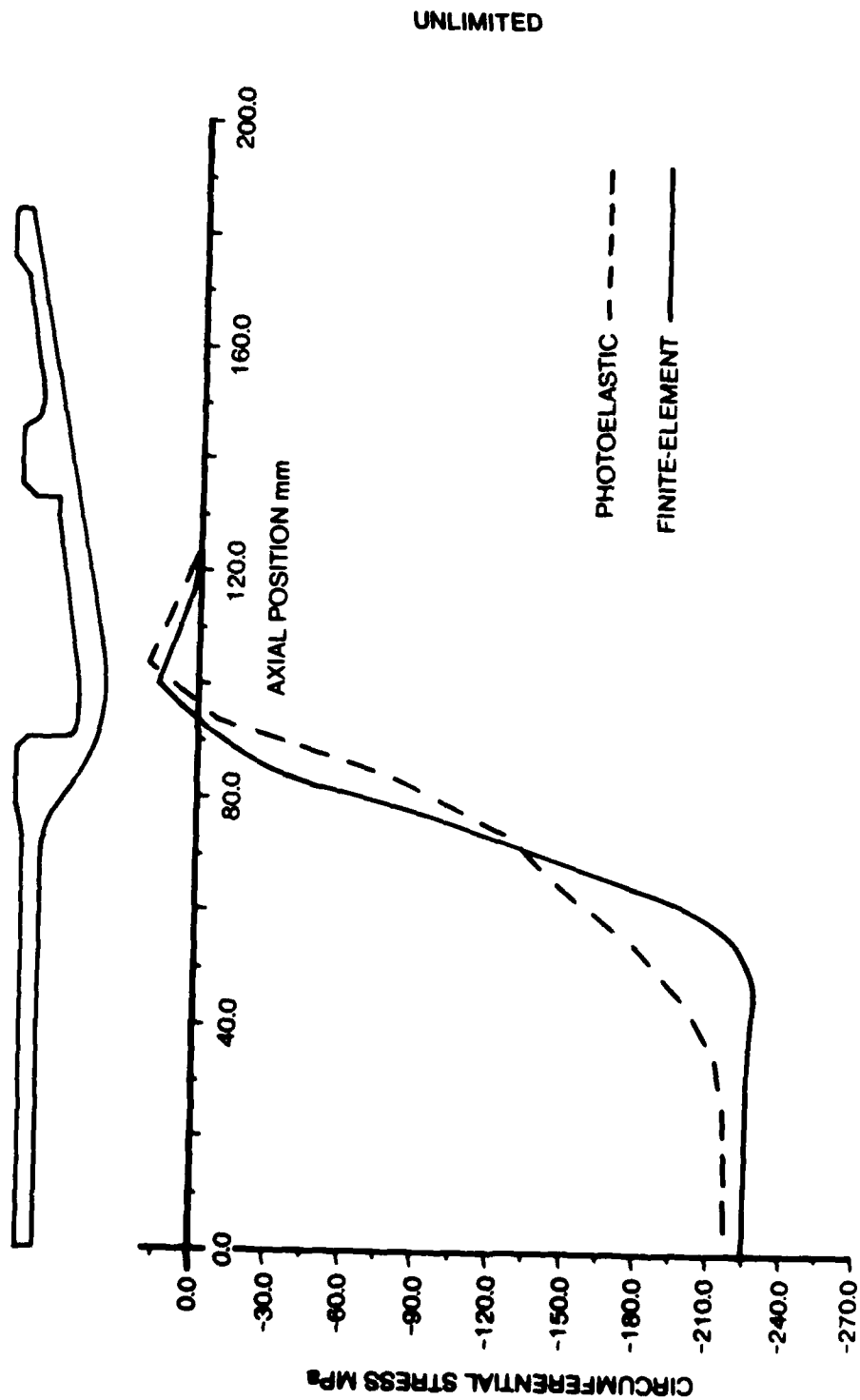


FIG. 6

FIG. 6 CIRCUMFERENTIAL STRESS vs AXIAL STATION: OVERWOUND STATE (INNER SURFACE)

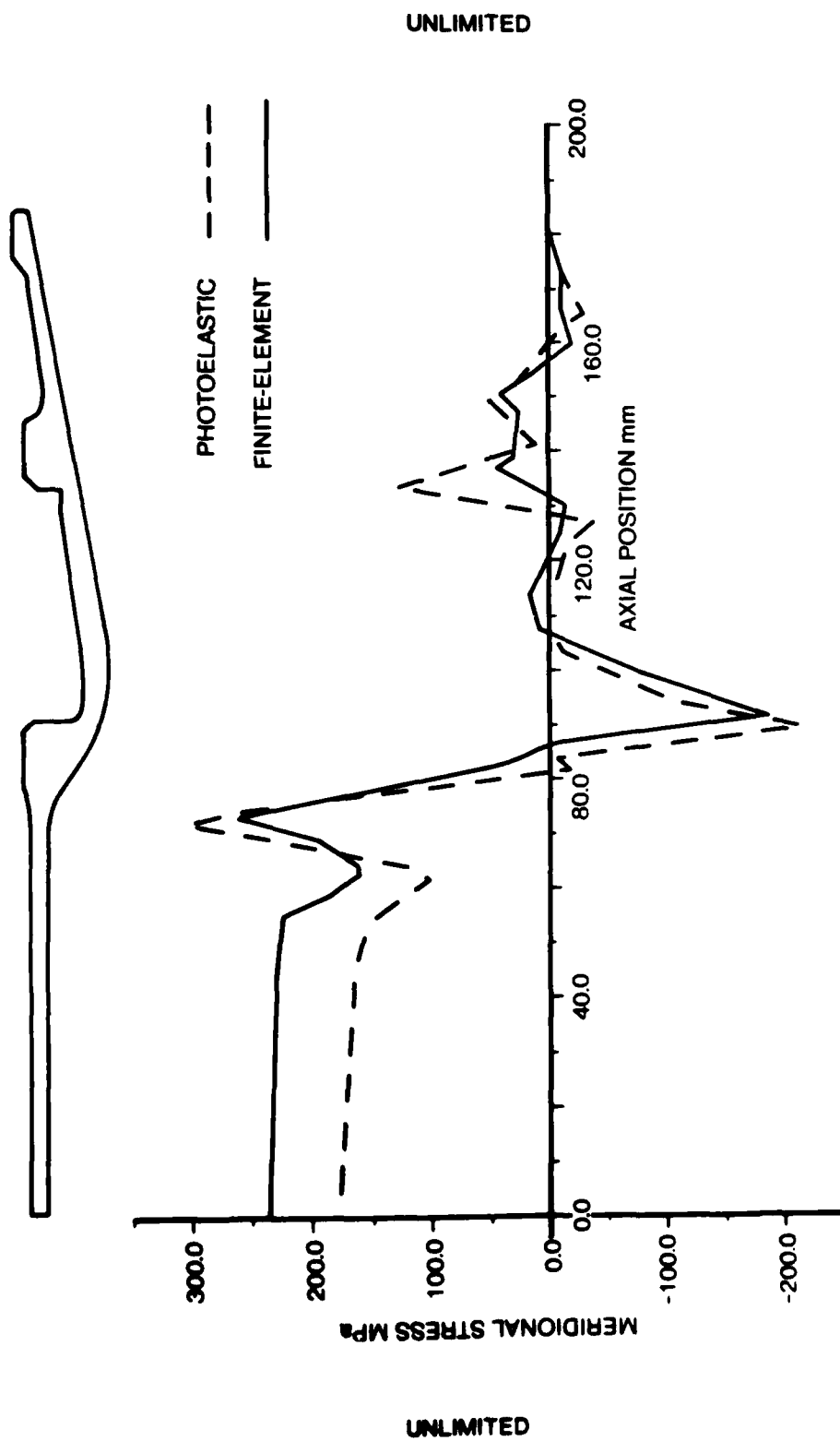


FIG. 7

FIG. 7 MERIDIONAL STRESS vs AXIAL STATION: INERTIA LOADING (INNER SURFACE)

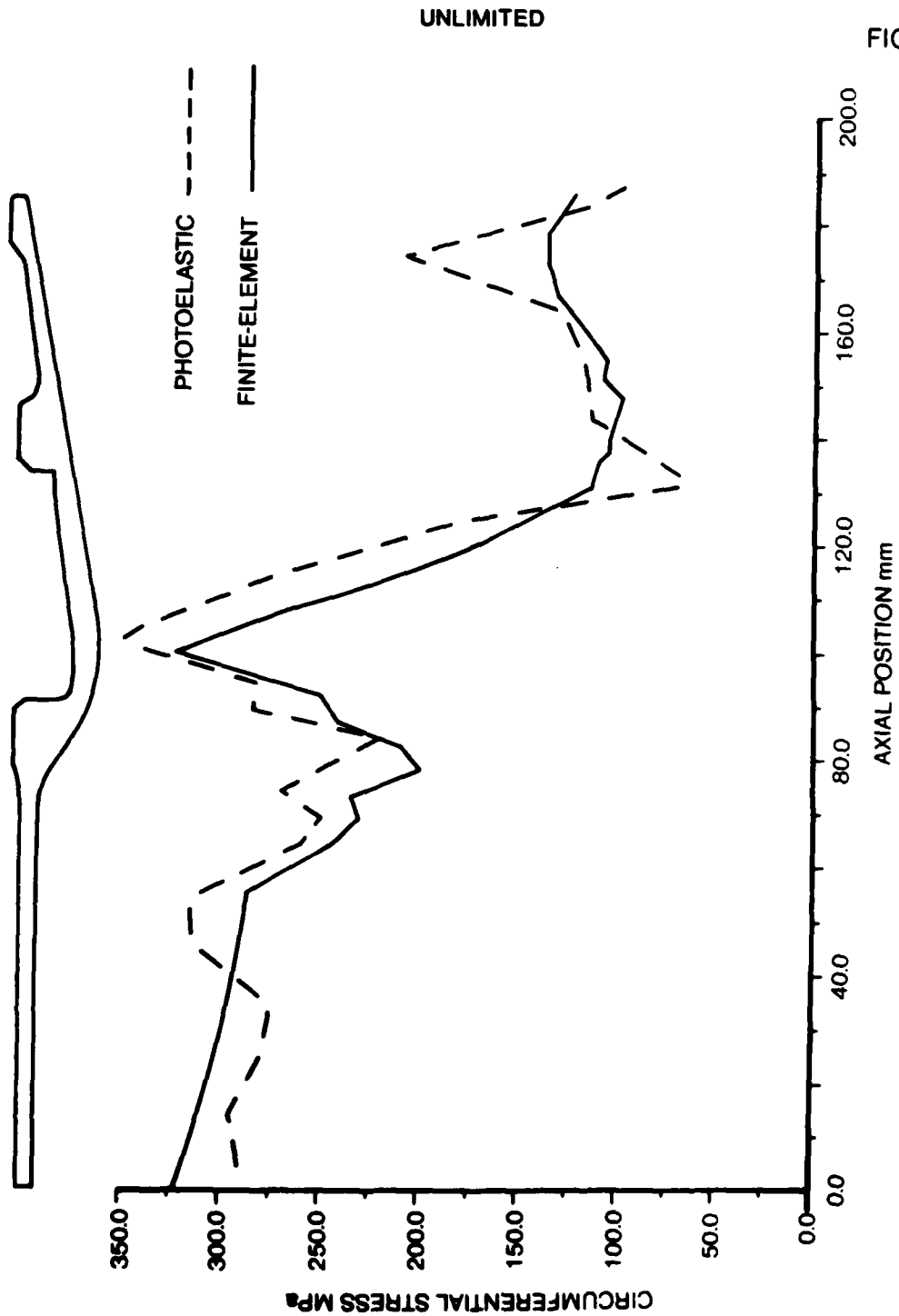


FIG. 8

FIG. 8 CIRCUMFERENTIAL STRESS vs AXIAL STATION: COMBINED LOADING (INNER SURFACE)

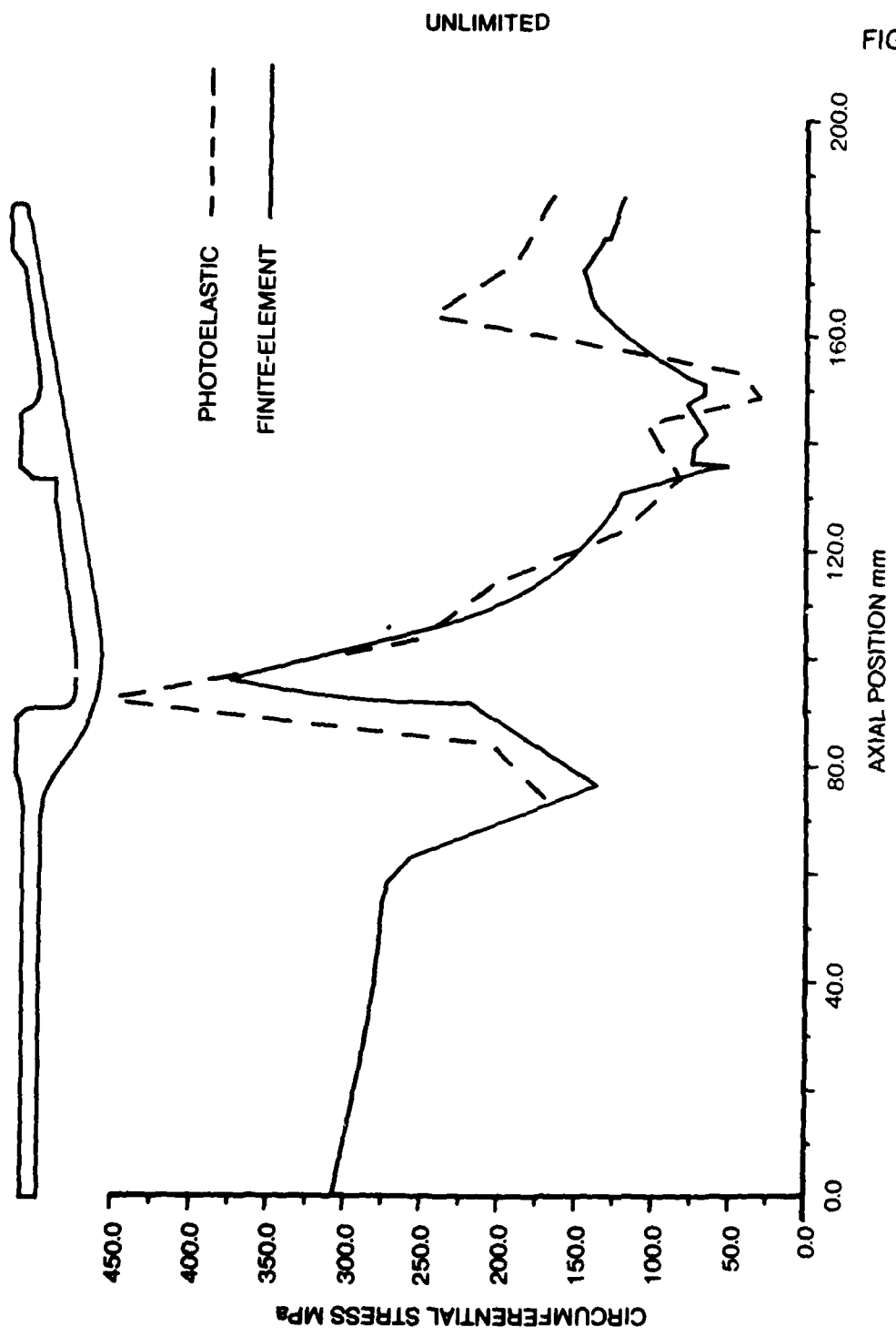


FIG. 9

FIG. 9 CIRCUMFERENTIAL STRESS vs AXIAL STATION: COMBINED LOADING (OUTER SURFACE)

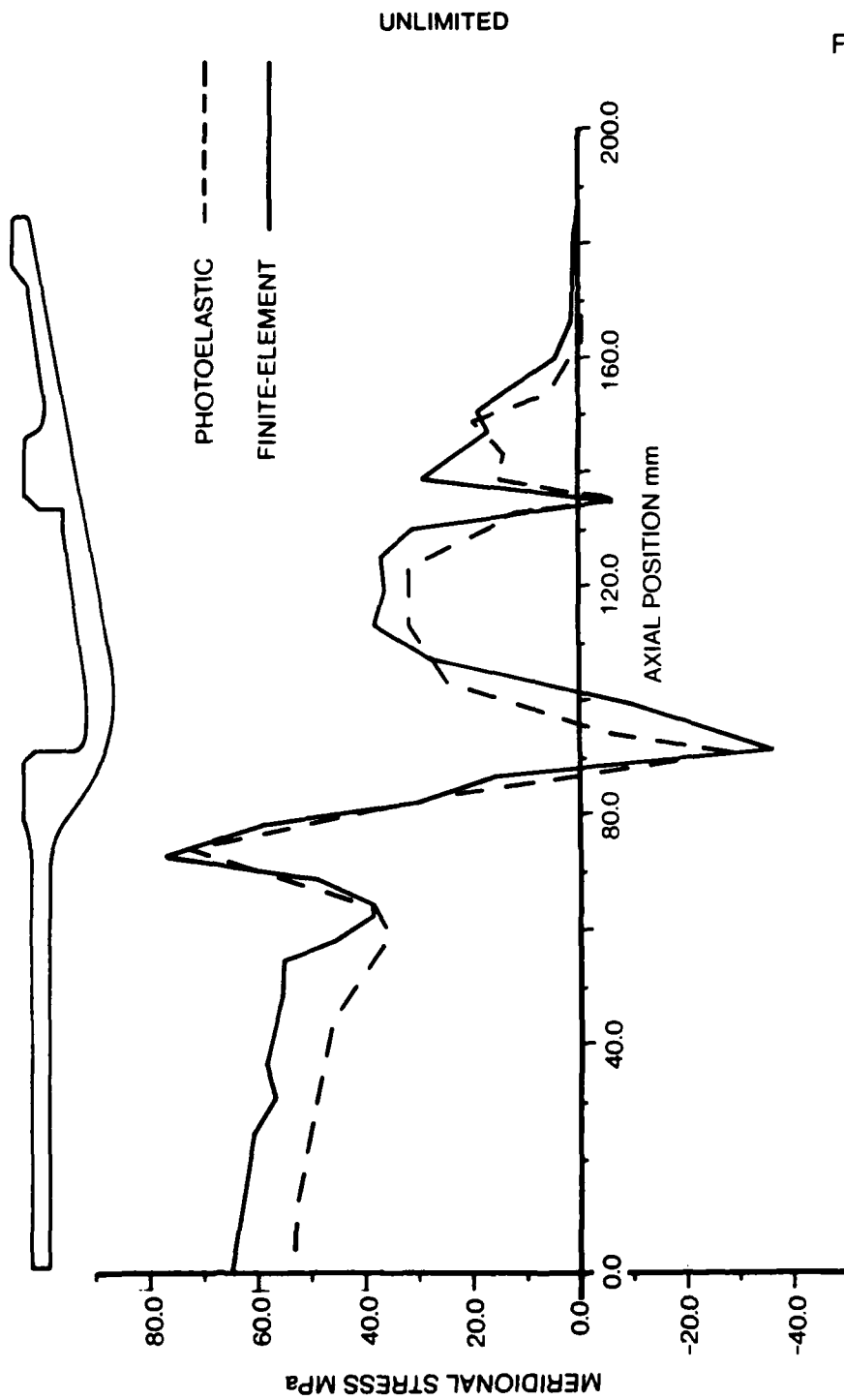


FIG. 10

FIG. 10 MERIDIONAL STRESS vs AXIAL STATION: COMBINED LOADING (INNER SURFACE)

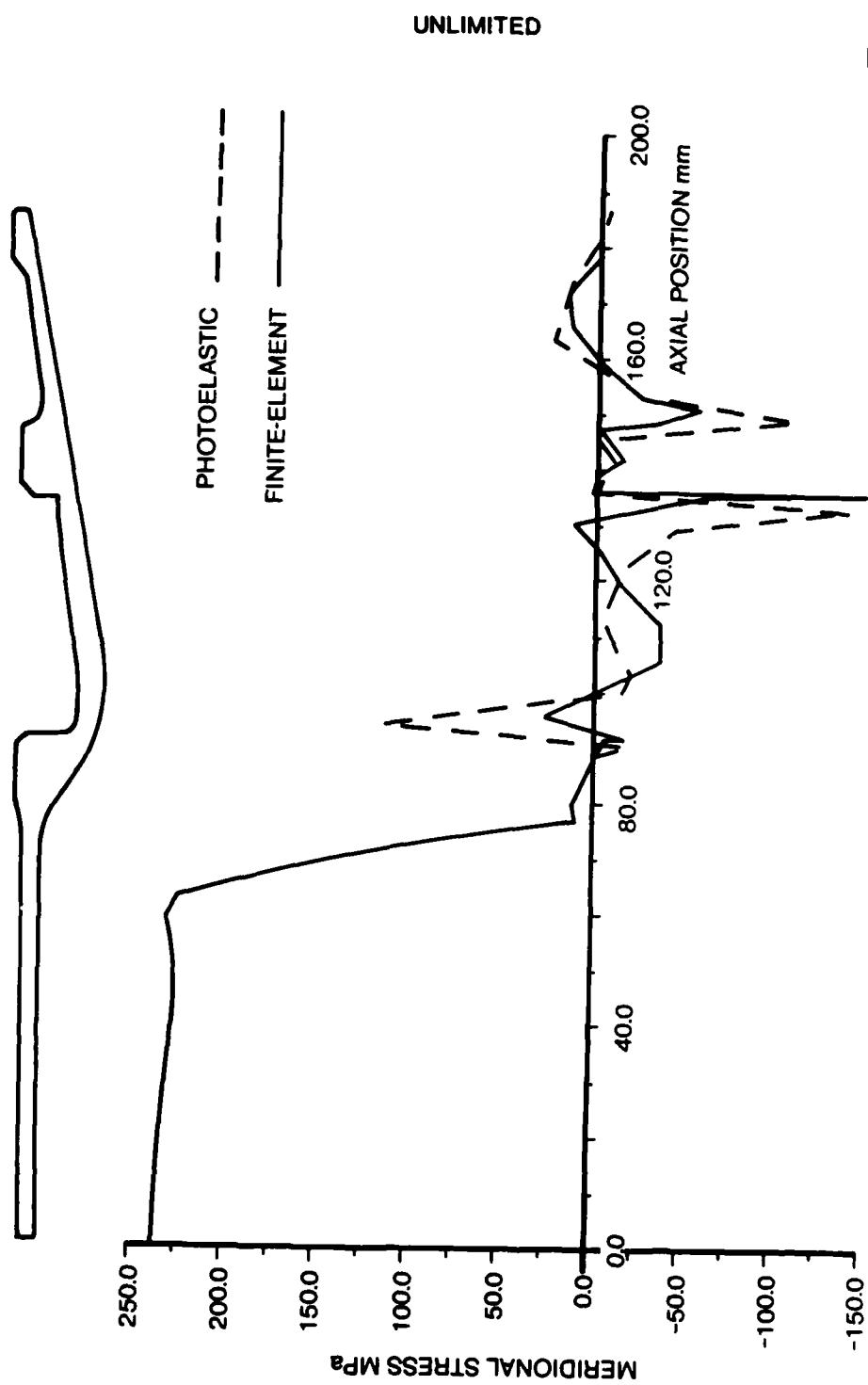


FIG. 11

FIG. 11 MERIDIONAL STRESS vs AXIAL STATION: COMBINED LOADING (OUTER SURFACE)

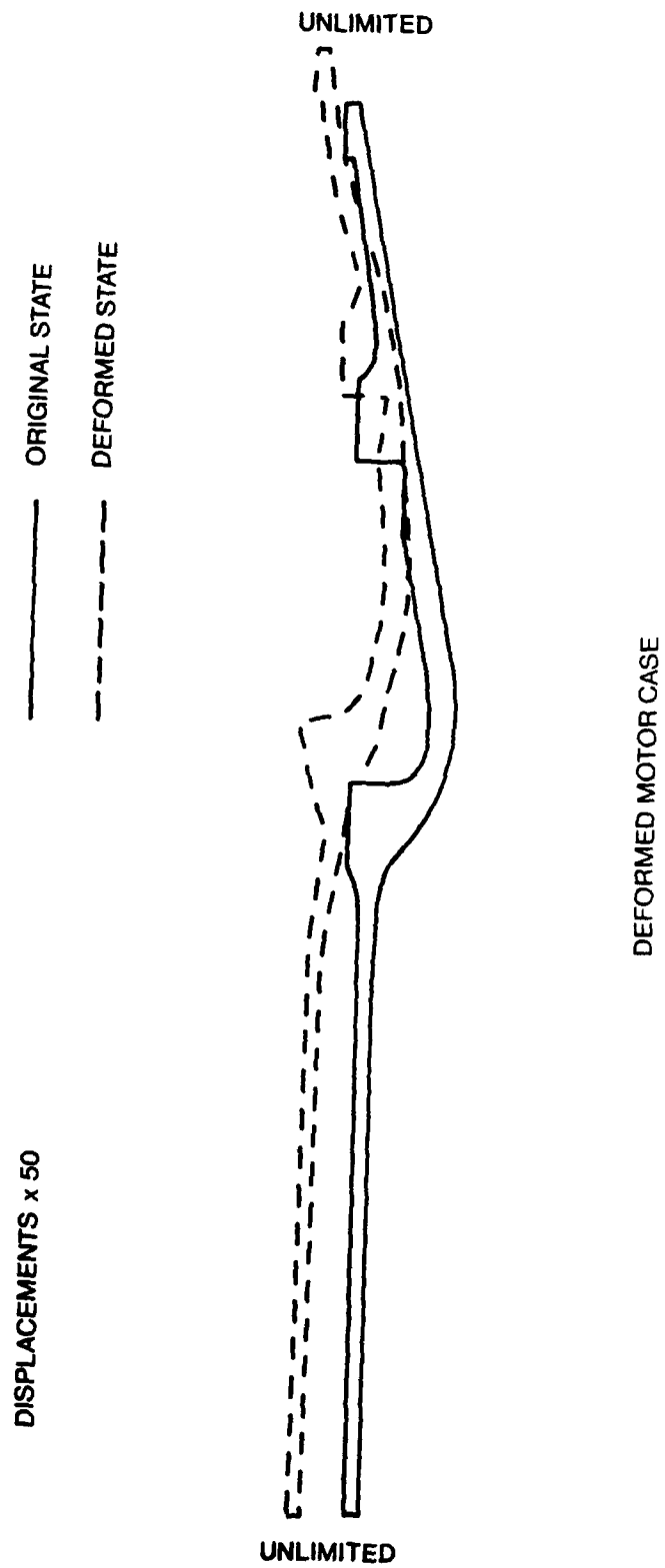


FIG. 12

FIG. 12 DEFORMED MOTOR CASE

UNLIMITED

ANNEX A

INTERFACE PRESSURE CALCULATION

The interface pressure (p_b) between the first fibre layer and the case consists of two components, one due to winding (p_{bw}) and one due to the application of the internal pressure (p_{bp}).

The winding-induced component p_{bw} can be readily obtained from the pre-stress produced during winding $\sigma_{\theta c}^{(n)}$ through the thin-walled cylinder equations in the form

$$p_{bw} = \frac{-\sigma_{\theta c}^{(n)} t_c}{R}, \quad (A1)$$

which, when using Equation 2 to eliminate $\sigma_{\theta c}^{(n)}$, modifies to:

$$p_{bw} = \frac{E_c \epsilon_w A F_1(A, n) t_c}{R} \quad (A2)$$

In principle it would also seem admissible to use the thin-walled cylinder approximations to calculate the pressure-induced interface pressure component p_{bp} to give

$$p_{bp} = p - p_{bw} - \frac{\sigma_{\theta c p}^{(n)} t_c}{R} \quad (A3)$$

and hence

$$p_b = p_{bw} + p_{bp} \quad (A4)$$

However, the thin-walled cylinder equations are approximations of the exact solution, as given by Lamé (Ref 14). Although the error in p_{bp} is consistent with these approximations, typically less than a few per cent, it has been found that under certain conditions considerable errors in the circumferential stress calculations can occur when this estimated value for p_{bp} is used. If an error analysis is performed for the circumferential stress σ_θ to assess the effects of small errors in p_{bp} on σ_θ (see Annex B) the following relationship can be derived

$$\frac{\Delta \sigma_\theta}{\sigma_\theta} = \frac{\Delta p_{bp}}{p_{bp} - p + \frac{p t_c}{R}} \quad (A5)$$

where $\Delta \sigma_\theta$ and Δp_{bp} are the respective errors in σ_θ and p_{bp} . For a thin-walled cylinder circumferentially reinforced with a fibre overwind the

UNLIMITED

interface pressure p_{bp} can approach the internal pressure p , resulting in the equation

$$\frac{\Delta\sigma_\theta}{\sigma_\theta} = \frac{R\Delta p_{bp}}{t_c p_{bp}} \quad (A6)$$

From the above equation it is evident that when p and p_{bp} are approximately equal the relative error in σ_θ is proportional to the relative error in p_{bp} with the constant of proportionality given by R/t_c . Since for thin-walled cylinders R/t_c is typically greater than ten it follows that small errors in the interface pressure predictions can induce large errors in the circumferential stress calculations.

If the interface pressure is significantly different from the internal pressure, as is the situation during winding, the relative errors in the interface pressure predictions are comparable to those of the circumferential stress calculations. It is for this reason that it is admissible to use the thin-walled cylinder approximations to calculate p_{bw} , ie Equation A2.

In view of the previous discussion it is essential therefore that the pressure-induced interface pressure p_{bp} is evaluated using the Lamé equations. Omitting details it can be easily shown from a compound cylinder analysis that the required interface pressure p_{bp} is obtained from

$$p_{bp} = p \frac{\left[\frac{2R_1^2}{E_c(R_b^2 - R_1^2)} + \frac{\nu_c(R_1^2 - R_e^2)}{E_c(R_b^2 - R_1^2)} \right]}{\left[\frac{R_b^2 + R_1^2}{E_c(R_b^2 - R_1^2)} + \frac{R_o^2 + R_b^2}{E_f(R_o^2 - R_b^2)} \right]} \quad (A7)$$

where R_1 and R_b are the internal and interface radii respectively of the metallic case and R_o is the external radius of the fibre-reinforced metallic rocket motor (ie $R_o = R_b + nt_f$).

UNLIMITED

ANNEX B

ERROR ANALYSIS

The Lamé equation for the circumferential stress at the outer surface of an internally and externally pressurised cylinder of inner radius R_i and outer radius R_b is given by (Ref 14)

$$\sigma_\theta = -p + (p - p_{bp}) \left[\frac{R_b^2 + R_i^2}{R_b^2 - R_i^2} \right] \quad (B1)$$

where p and p_{bp} denote the internal and external pressures respectively. If the internal pressure is assumed fixed, but p_{bp} is subject to some small error Δp_{bp} , it follows from Equation B1 that the corresponding error in σ_θ , ie $\Delta \sigma_\theta$, is

$$\Delta \sigma_\theta = -\Delta p_{bp} \left[\frac{R_b^2 + R_i^2}{R_b^2 - R_i^2} \right] \quad (B2)$$

The above error can now be assessed relative to the actual stress by dividing Equation B2 by B1 to give

$$\frac{\Delta \sigma_\theta}{\sigma_\theta} = \frac{-\Delta p_{bp} \left[\frac{R_b^2 + R_i^2}{R_b^2 - R_i^2} \right]}{-p + (p - p_{bp}) \left[\frac{R_b^2 + R_i^2}{R_b^2 - R_i^2} \right]} \quad (B3)$$

Introducing the following thin-walled cylinder approximation

$$\frac{R_b^2 + R_i^2}{R_b^2 - R_i^2} \div \frac{R}{t_c} \quad (B4)$$

reduces Equation B3 to the simple form

$$\frac{\Delta \sigma_\theta}{\sigma_\theta} = \frac{\Delta p_{bp}}{p_{bp} - p + \frac{t_c p}{R}} \quad (B5)$$

From the above equation the effect of errors in p_{bp} on σ_θ can be easily assessed. If the difference between p_{bp} and p is large then the relative error in σ_θ is comparable to the relative error in p_{bp} . On the other

81
UNLIMITED

UNLIMITED

hand if p_{bp} equals p then the relative error in σ_θ becomes proportional to the relative error in p_{bp} with the constant of proportionality given by R/t_c . Since for thin-walled cylinders R/t_c will always be significantly greater than unity the relative error in σ_θ for a small error in p_{bp} can become large.

B2
UNLIMITED

REPORT DOCUMENTATION PAGE

(Notes on completion overleaf)

Overall security classification of sheet UNLIMITED

(As far as possible this sheet should contain only unclassified information. If it is necessary to enter classified information, the box concerned must be marked to indicate the classification eg (S), (C), or (S)).

1. ERIC Reference (if known)	2. Originator's Reference Report 4/86	3. Agency Reference	4. Report Security Classification UNLIMITED
5. Originator's Code (if known) 7699000H	6. Originator (Corporate Author) Name and Location Ministry of Defence Royal Armament Research and Development Establishment		
5A. Sponsoring Agency's Code (if known)	6A. Sponsoring Agency (Contract Authority) Name and Location		
7. Title Structural Analysis of Fibre-Reinforced Metallic Rocket Motor Cases Using Finite-Element and Photoelastic Techniques			
7A. Title in Foreign Language (in the case of translation)			
7B. Presented at (for conference papers). Title, place and date of conference			
8. Author 1, Surname, initials Margetson, J.	9A. Author 2 Groves, A.	9B. Authors 3, 4...	10. Date pp ref December 1986 29 14
11. Contract number and Period		12. Project	13& 14 Other References.
15. Distribution statement			
Descriptors (or keywords) Rocket engines, Fiber composites, Fiber laminates,	Reinforcement, (structures), Filaments, wound materials, Composite materials, Structural analysis,	Finite element analysis Photoelastic analysis	
<p>Abstract Stress analysis procedures are presented for fibre-reinforced metallic rocket motor cases using finite-element and photoelastic techniques. These techniques enable analyses of the initial winding process, inertia and pressurisation due to firing to be performed. Certain simplifications and assumptions are introduced to resolve the complicating effects of the fibre overwind and the in-flight loadings. A comparison between the two methods for a typical motor is considered.</p> <p><i>Keywords:</i> _____</p>			

END

DATE
FILMED

7-87